



This is a repository copy of *Semiconductor nanostructure quantum ratchet for high efficiency solar cells*.

White Rose Research Online URL for this paper:
<http://eprints.whiterose.ac.uk/142166/>

Version: Published Version

Article:

Vaquero-Stainer, A., Yoshida, M., Hylton, N.P. et al. (9 more authors) (2018)
Semiconductor nanostructure quantum ratchet for high efficiency solar cells.
Communications Physics, 1. 7. ISSN 2399-3650

<https://doi.org/10.1038/s42005-018-0007-6>

Reuse

This article is distributed under the terms of the Creative Commons Attribution (CC BY) licence. This licence allows you to distribute, remix, tweak, and build upon the work, even commercially, as long as you credit the authors for the original work. More information and the full terms of the licence here:
<https://creativecommons.org/licenses/>

Takedown

If you consider content in White Rose Research Online to be in breach of UK law, please notify us by emailing eprints@whiterose.ac.uk including the URL of the record and the reason for the withdrawal request.



eprints@whiterose.ac.uk
<https://eprints.whiterose.ac.uk/>

ARTICLE

DOI: 10.1038/s42005-018-0007-6

OPEN

Semiconductor nanostructure quantum ratchet for high efficiency solar cells

Anthony Vaquero-Stainer¹, Megumi Yoshida¹, Nicholas P. Hylton¹, Andreas Pusch¹, Oliver Curtin¹, Mark Frogley³, Thomas Wilson¹, Edmund Clarke ², Kenneth Kennedy², Nicholas J. Ekins-Daukes ¹, Ortwin Hess ¹ & Chris C. Phillips¹

Conventional solar cell efficiencies are capped by the ~31% Shockley–Queisser limit because, even with an optimally chosen bandgap, some red photons will go unabsorbed and the excess energy of the blue photons is wasted as heat. Here we demonstrate a “quantum ratchet” device that avoids this limitation by inserting a pair of linked states that form a metastable photoelectron trap in the bandgap. It is designed both to reduce non-radiative recombination, and to break the Shockley–Queisser limit by introducing an additional “sequential two photon absorption” (STPA) excitation channel across the bandgap. We realise the quantum ratchet concept with a semiconductor nanostructure. It raises the electron lifetime in the metastable trap by $\sim 10^4$, and gives a STPA channel that increases the photocurrent by a factor of ~50%. This result illustrates a new paradigm for designing ultra-efficient photovoltaic devices.

¹The Blackett Laboratory, Department of Physics, Imperial College London, London SW7 2AZ, UK. ²Department of Electronic and Electrical Engineering, University of Sheffield, Sheffield S1 3JD, UK. ³Diamond Light Source Limited, Harwell Science and Innovation Campus, Didcot OX11 0DE Oxfordshire, UK. Correspondence and requests for materials should be addressed to C.C.P. (email: chris.phillips@imperial.ac.uk)

Intermediate band (IB) cells^{1,2} have recently been studied as a way of beating the $\sim 31\%$ Shockley-Queisser (SQ) limit³. They work by placing an IB level in the bandgap that introduces a parallel excitation channel, allowing the sequential-two-photon-absorption (STPA) of sub-bandgap energy photons. A number of practical implementations based on well-established semiconductor nanostructure fabrication technologies, including quantum dots⁴, and superlattices⁵ have been reported. However, the short IB lifetime⁶ means they also induce high levels of Shockley-Read-Hall interband recombination⁷ that lower the cell voltage. The theoretical “quantum ratchet” (QR) concept⁸ has been proposed to circumvent this problem.

This QR approach (Fig. 1) introduces two states^{6,8} lying in the bandgap. The upper one (intermediate band, IB) is optically coupled only to the valence band (VB) and the lower one (Ratchet band, RB) is optically coupled only to the conduction band (CB). A rapid irreversible scattering process links the two, so their carrier populations are characterised by the same quasi-Fermi level. In spite of the energy, ΔE , lost in the IB \Rightarrow RB transition, idealised global optimisation models⁸ predict limiting QR device efficiencies of $>46\%$ ($\Delta E \sim 270$ meV) at one sun and $\sim 63\%$ at full concentration ($\Delta E = 0$). Both are significantly better than the corresponding SQ limits.

Our implementation (Fig. 1b) uses a quantum well (QW) interband transition for the VB \Rightarrow IB stage, transport through a QW superlattice for the IB \Rightarrow RB ratchet stage, followed by an intraband bound-to-continuum intersubband (ISBT) transition between two electron states for the RB \Rightarrow CB stage. A test device was designed in order to isolate the photocurrent contribution of the STPA channel experimentally. The bandgap corresponding to the VB \Rightarrow IB transition (taking place in the 25 nm thick $\text{In}_{0.05}\text{Ga}_{0.95}\text{As}$ layer adjacent to the QW's), was designed to be the lowest energy interband transition in the multilayer, so that it could be driven without generating photocarriers anywhere else. In order to optimise the fraction of IB electrons being scattered into the metastable RB state, rapid IB \Rightarrow RB scattering was facilitated by designing the QW superlattice so that neighbouring wells had confined state energies separated by an optical phonon energy⁹. The device was packaged in a bevelled configuration to allow the RB \Rightarrow CB transition to be driven with p-polarised light, as is required by the dipole selection rules for ISBT's¹⁰.

Using high speed, time resolved STPA photocurrent measurements, we find here that the QR design increases the electron lifetime in the RB state by $\sim 10^4$ to ~ 10 μs . It introduces an STPA channel that increases the photocurrent by a factor of $\sim 50\%$.

Results

STPA photocurrent spectral characteristics. The 100 μm diameter device was cooled to ~ 14 K and illuminated with two independently tuneable laser pulse trains at a 100 kHz repetition rate. The VB \Rightarrow IB transition was resonantly driven with a $\lambda = 850$ nm, ~ 150 ps pulse filtered out from an optical fibre supercontinuum source, with a bandwidth of 2.5 nm and a pulse power/energy up to 2.5 W/0.4 nJ. The RB \Rightarrow CB transition was driven with a bank of tuneable quantum cascade laser (QCL) diodes, giving $6 \mu\text{m} < \lambda < 10 \mu\text{m}$ pulses ~ 100 ns long and ~ 800 μW CW power. This corresponded to a mean pulse power/energy of up to approximately 80 mW/8 nJ.

The two pulse trains could be mechanically chopped (at ~ 465 Hz for the VB \Rightarrow IB supercontinuum beam and ~ 535 Hz for the RB \Rightarrow CB QCL beam) to measure their single photon contribution to the photocurrent with independent lock-in amplifiers. The QCL beam generated no detectable single photon photocurrent, whereas the supercontinuum beam generated a photo current I–V

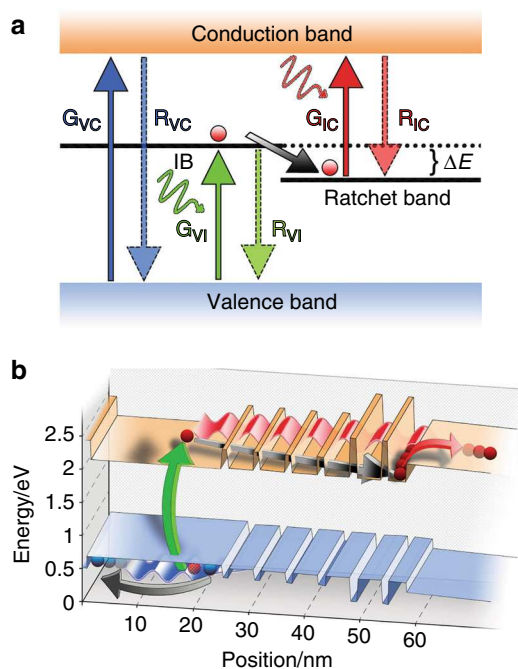


Fig. 1 Schematic of the “quantum ratchet” concept. **a** The absorbing section of a photovoltaic (PV) device is structured to allow both direct interband absorption (blue arrows) between the conduction (CB) and valence bands (VB), and an additional “sequential-two-photon-absorption” (STPA) channel that is designed to add to the photocurrent without sacrificing the cell voltage. It achieves this by having two reversible optically allowed transitions denoted by the green arrow (VB to intermediate band (IB)) and the red arrow (ratchet band (RB) to CB) that are separated by an irreversible IB to RB ratchet transition (grey arrow to the right). **b** Quantum ratchet device implementation used here. A QW superlattice provides the ratchet, as photoelectrons cascade to the right down a series of confined electron states. The device is designed so that the lowest energy interband transition pumps carriers into states at the left hand end of the ratchet, and an intersubband transition, (red arrow) is required to lift them out or the trapped state at the right hand end of the ratchet to contribute to the photocurrent

curve with a pronounced low-current plateau in the 0.4–0.8 V bias range, indicative of the QR action (Supplementary Note 1).

In common with IB cell devices based on semiconductor heterostructures the electronic transport in our device is temperature sensitive and so the STPA measurements must be done in a way that avoids artefacts due to sample heating. STPA experiments presented in the literature have used either CW sources^{4,5,11}, or ones that are chopped at a low fixed frequency, and thermal effects have been shown to give changes in photocurrent at the 10's % level (see ref. 12 and supplementary material therein). These thermal artefacts are avoidable by modulating the illumination sources at rates that are fast compared with the systems' thermal time constant. The fact that this has been achieved can be checked by verifying that the STPA signal is independent of the modulation frequencies. One of the unique aspects of the present work is that we used a frequency mixing circuit to drive a third lock-in amplifier at a frequency corresponding to the difference between the modulation frequencies of the two laser beams. This is done in order to isolate the fast contribution to the photocurrent that originates from the STPA excitation process.

In the lower-noise, mechanically chopped experimental configuration, the frequency mixing was achieved with a custom

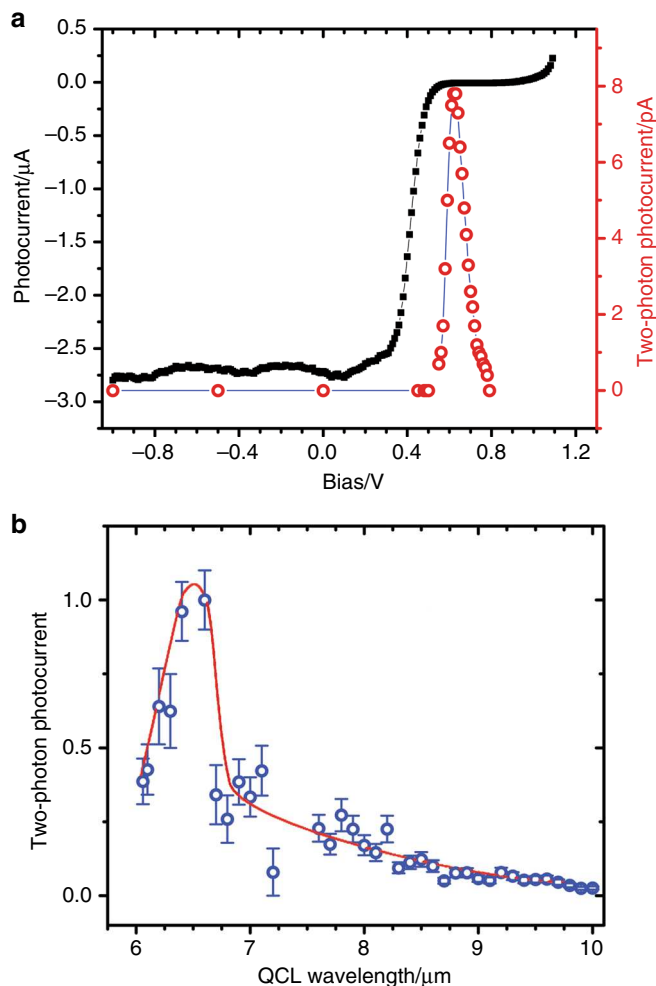


Fig. 2 STPA photocurrent. **a** Filled squares: 14 K photo current-voltage curve for the quantum ratchet device, showing the 0.4–0.8 V current plateau where carriers are effectively trapped in the RB state. Circles, bias dependence of the STPA photocurrent, peaking at ~ 0.62 V. At lower biases the field in the QW superlattice is insufficient to separate the photocarriers into the RB state, and at higher biases the carriers can tunnel out of the RB state without two photon excitation. **b** Spectral dependence of the 14 K STPA signal on mid-IR wavelength when pumped with a fixed $\lambda = 850$ nm interband excitation beam. Error bars correspond to the standard error of the mean of 10 consecutive measurements

made digital electronic circuit. However, we also checked that the signal was unchanged when we took the experiment to the highest frequency available. This was achieved by mixing the (fixed) 100 kHz modulation frequency of the supercontinuum source with an 80 kHz pulse train from electronically triggered QCL's in an analogue diode mixer, and lock-in detecting at the ~ 20 kHz difference frequency. This gave a STPA signal that was the same to within experimental error as the much slower mechanically chopped experiment. However, for technical reasons the mechanically chopped setup gave a better signal-to-noise ratio and was used for all the data presented here. At all times, the STPA signal disappeared when either laser was blocked, and no STPA signals were found with a control device that was grown with a large bandgap layer inserted into the QW superlattice in a way that was designed to block the $\text{IB} \Rightarrow \text{RB}$ transport.

The 14 K photocurrent I–V curve (Fig. 2) shows an almost zero-current plateau on the 0.4–0.8 V bias range, consistent with

efficient charge-trapping in the RB state, (Supplementary Note 1). Only samples showing this plateau gave an STPA photocurrent signal and it was only ever non-zero within this bias range. At lower forward biases the field is enough to extract electrons from the RB state into the CB one (as signified by a pronounced increase in the $\text{VB} \Rightarrow \text{IB}$ single photon photocurrent at this bias, see Supplementary Note 1). At higher forward biases, the $\text{IB} \Rightarrow \text{RB}$ ratchet is too shallow to scatter the IB electrons quickly enough into the RB state to collect a significant fraction of them before they recombine back into the VB state.

Tuning the QCL's revealed a peaked spectral response (Fig. 2b) in the STPA photocurrent, centred at $\lambda \sim 6.5 \mu\text{m}$, with a wavelength full-width-half-maximum of $\Delta\lambda \sim 1 \mu\text{m}$. Rotating the polarisation plane of the QCL revealed the transition to be p-polarised at a level of more than 28:1 (limited by measurement noise), and its energy corresponded well with the $\lambda \sim 6.4 \mu\text{m}$ modelled transition energy of the $\text{RB} \Rightarrow \text{CB}$ transition.

Intensity dependence of the STPA photocurrent. The STPA photocurrent was linear in $\text{RB} \Rightarrow \text{CB}$ QCL intensity over the accessible range (Fig. 3), but it saturated readily, and even decreased with $\sim 30\%$ of the laser intensity that was available for the $\text{VB} \Rightarrow \text{IB}$ excitation. Order of magnitude estimates (Supplementary Note 2) indicate that at this stage electron space charge accumulation in the RB state would start to generate enough field to flatten the $\text{IB} \Rightarrow \text{RB}$ ratchet potential. This would reduce its ability to quickly separate electron-hole pairs generated by the $\text{VB} \Rightarrow \text{IB}$ laser before they have time to recombine.

Time resolved measurements of the RB level lifetime. Time resolved studies were initially done with an optical delay line capable of generating a delay of up to 2 ns between the pulse trains, but no time dependence in the signals could be detected on these timescales. All the results reported here were obtained by electronically varying the delay between the pulse trains on a much longer timescale, one that was limited by the $10 \mu\text{s}$ pulse repetition rate.

The lifetime measurements (Fig. 4) showed a decay time that was comparable with the $10 \mu\text{s}$ laser repetition rate, i.e., a $\sim 10^4$ fold enhancement over the approximately nanosecond values typical of interband recombination in direct-gap QW materials. Its bias (Fig. 4a) and temperature (Fig. 4b) dependencies both showed an approximately reciprocal relationship with those of the STPA photocurrent, furthering the argument that the lifetime enhancement in the RB state is key to achieving effective two-photon absorption. As the device temperature is raised from 14 to 50 K, (by which time the RB lifetime reduces from ~ 10 to $\sim 0.8 \mu\text{s}$), the time averaged STPA photocurrent has dropped by a factor of ~ 3 before becoming lost in the measurement noise. The thermally activated lifetime reduction correlated with the disappearance of the current plateau in the I–V curves.

Discussion

The modelled 10^{-9} – 10^{-10} quantum mechanical overlap factor between the IB and RB wave functions is approximately six decades less than the inverse of the measured $\sim 10^4$ lifetime enhancement factor. This suggests that the measured lifetimes are limited by a thermally activated process. Estimates of the effects of carrier screening, and band filling (Supplementary Note 2) suggest that the former flattens out the ratchet potential at carrier densities roughly a decade lower than those when the Fermi energy starts to rise significantly in the RB, so we surmise screening it is the dominant contribution to the saturation effect in Fig. 3a. When the saturation sets in (at ~ 0.25 nJ/pulse) we estimate a RB occupancy of $\sim 1.3 \times 10^{11} \text{ cm}^{-2}$, which compares

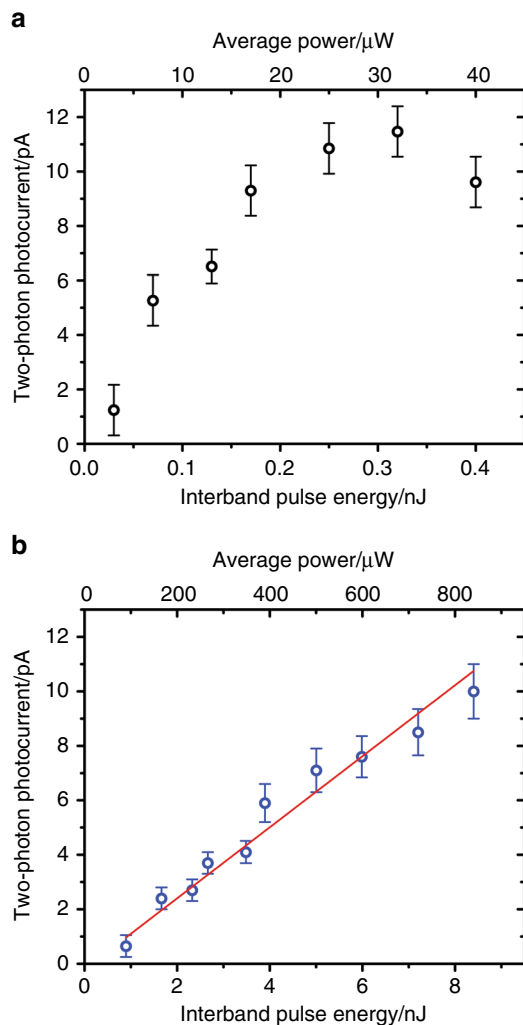


Fig. 3 Intensity dependence of the STPA photocurrent. **a** STPA contribution to the photocurrent as a function of $\lambda = 850$ nm interband beam intensity, and **b** STPA contribution to the photocurrent $\lambda = 6.5$ μm intraband beam intensity. For each curve the intensity of the other beam was fixed at the value corresponding to the maximum STPA response. The saturation effect in (**a**) corresponds to approximate estimates of the excitation rate needed to generate a 2 D electron space charge density in the RB that is high enough to screen out the potential drop along the ratchet scattering channel. Error bars correspond to the standard error of the mean of 10 consecutive measurements

with the $\sim 6 \times 10^{11} \text{ cm}^{-2}$ needed to completely screen out the ratchet potential (Supplementary Note 2).

At the optimum bias (0.63 V) the STPA channel increases the time-averaged photocurrent by 0.5% of the single photon current generated by the interband pumping alone, (Supplementary Note 3). However, ISBT lifetimes lie typically in the sub-ps range¹³, so it is likely that all the STPA photocurrent occurs within the ~ 100 ns QCL pulse; correcting for the 100:1 duty cycle in the QCL pulse train implies an actual STPA photocurrent that is $\sim 50\%$ of the single photon value.

A quantitative analysis (Supplementary Note 3) implies a reasonable IB-RB scattering efficiency of $\sim 57\%$. The low overall power conversion rates are predominantly due to combination of a low ($\sim 7.4 \times 10^{-5}$) optical coupling factor to the RB-CB transition in the present experimental geometry, and to a low escape probability into the CB ($\sim 3.9 \times 10^{-5}$) for electrons excited into the upper level of the RB QW. Based on the literature on QW

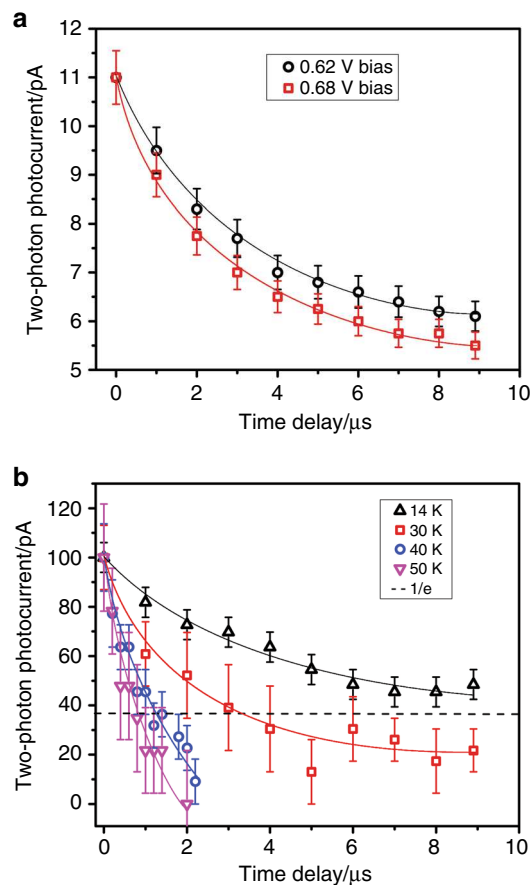


Fig. 4 Measured decay time of the STPA signal. **a** As a function of sample bias at 14 K, **b** As a function of temperature, at a sample bias of 0.62 V. The solid lines are guides to the eye, and the curves have been normalised to the zero time delay value. Error bars correspond to the standard error of the mean of 10 consecutive measurements

infrared detectors (QWIP's), both of these can be increased towards unity. A variety of surface patterning techniques have been demonstrated¹⁴ that couple normally incident mid-IR light with efficiencies up to $\sim 90\%$ to the vertically polarised ISBT. The escape probability has been shown to be exponentially dependent on field¹⁵, and QWIPs routinely achieve values close to 100% by utilising fields that are ~ 40 times higher than the $\sim 4 \times 10^6 \text{ Vm}^{-1}$ present in the RB region of this test device.

The present design uses a materials system chosen because of its mature growth technology, and it operates with transition energies which are lower than would be needed to beat the SQ limit in practice. Future experiments, with wider bandgap semiconductor materials⁹ would be needed to match the transition energies on the ratchet device to the spectral content of the solar spectrum. At the same time, this would increase the trapping energy for the RB level, to give higher temperature operation.

In conclusion, we believe that this proof-of-principle result, and the dramatic ($\times 10^4$) lifetime enhancements achieved, argue the case for the quantum ratchet concept having an important role in a new family of ultra-efficient PV devices.

Methods

Device design and fabrication. The device was grown by Molecular Beam Epitaxy on an undoped GaAs substrate (Fig. 5), chosen to be transparent to the QCL laser beam. The QR portion (Table 1, layers 4–15) consists of an Al(GaAs)/GaAs QW superlattice structure embedded in a p–n junction. It is capped with a 25 nm layer of $\text{In}_{0.05}\text{Ga}_{0.95}\text{As}$, which has the lowest bandgap in the whole structure (appearing as the $\lambda \sim 850$ nm eV PL peak in Supplementary Figure 1(b)), so that a suitably

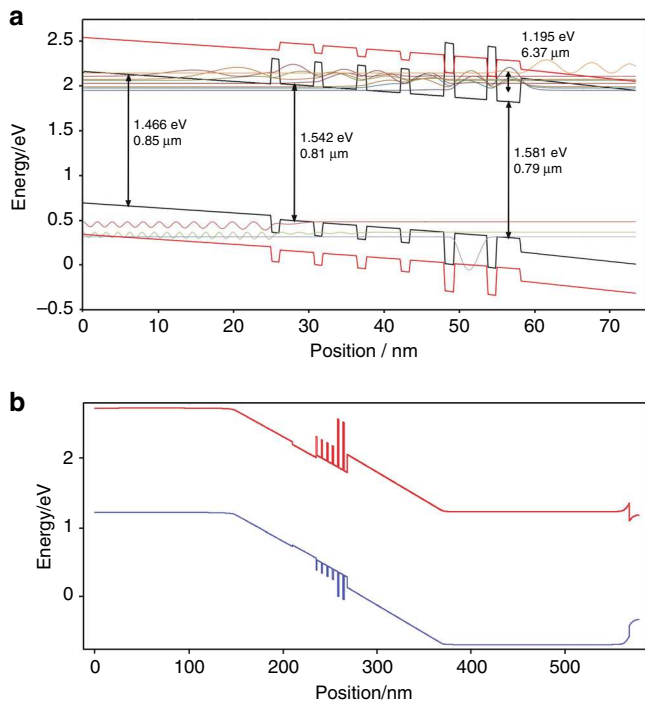


Fig. 5 Device band structure. **a** Band structure of the “quantum ratchet” portion of the device, comprising six quantum wells with their electron confined states designed to form a cascade of states, each separated by an optical phonon energy. Black lines, Γ -point band edge, red lines X-point band edge. **b** Complete Γ -point structure of the device, with the QR stage incorporated in a normal p-n diode

Table 1 Layer structure of the quantum ratchet device

Layer number	Thickness (nm)	Material	Doping (cm^{-3})
1	150	GaAs contact	10^{18} p-type
2	50	GaAs	ud
3	25	$\text{In}_{0.05}\text{Ga}_{0.95}\text{As}$	ud
4	1.1	$\text{Al}_{0.3}\text{Ga}_{0.7}\text{As}$	ud
5	4.6	GaAs	ud
6	1.1	$\text{Al}_{0.3}\text{Ga}_{0.7}\text{As}$	ud
7	4.6	GaAs	ud
8	1.2	$\text{Al}_{0.3}\text{Ga}_{0.7}\text{As}$	ud
9	4.6	GaAs	ud
10	1.2	$\text{Al}_{0.3}\text{Ga}_{0.7}\text{As}$	ud
11	4.6	GaAs	ud
12	1.3	$\text{Al}_{0.7}\text{Ga}_{0.3}\text{As}$	ud
13	4.4	GaAs	ud
14	1.2	$\text{Al}_{0.7}\text{Ga}_{0.3}\text{As}$	ud
15	3.2	GaAs	ud
16	100	$\text{Al}_{0.3}\text{Ga}_{0.7}\text{As}$	ud
17	200	$\text{Al}_{0.3}\text{Ga}_{0.7}\text{As}$	2×10^{18} n-type
18	400	GaAs contact	2×10^{18} n-type
19	buffer	GaAs	ud
20	wafer	GaAs	ud

tuned laser can excite electron hole pairs only in this layer. The excited electrons are then scattered down through a cascade of coupled states that are confined in successive wells of the QW superlattice, into the “Ratchet Band” (RB) state in the final QW. The holes are extracted from the $\text{In}_{0.05}\text{Ga}_{0.95}\text{As}$ layer into the p-GaAs capping layer.

The cascade scattering rate is maximised by designing each confined electron state to be separated from its neighbour by an optical phonon energy. Towards the end of the cascade, the Aluminium fraction in the barriers is increased to 0.7 to increase the electron trapping in the RB state and thereby increase the likelihood of STPA. From the RB state a second, mid-infrared, photon is required to excite the electron into the continuum of intrinsic bulk $\text{Al}_{0.3}\text{Ga}_{0.7}\text{As}$ to register a photo-

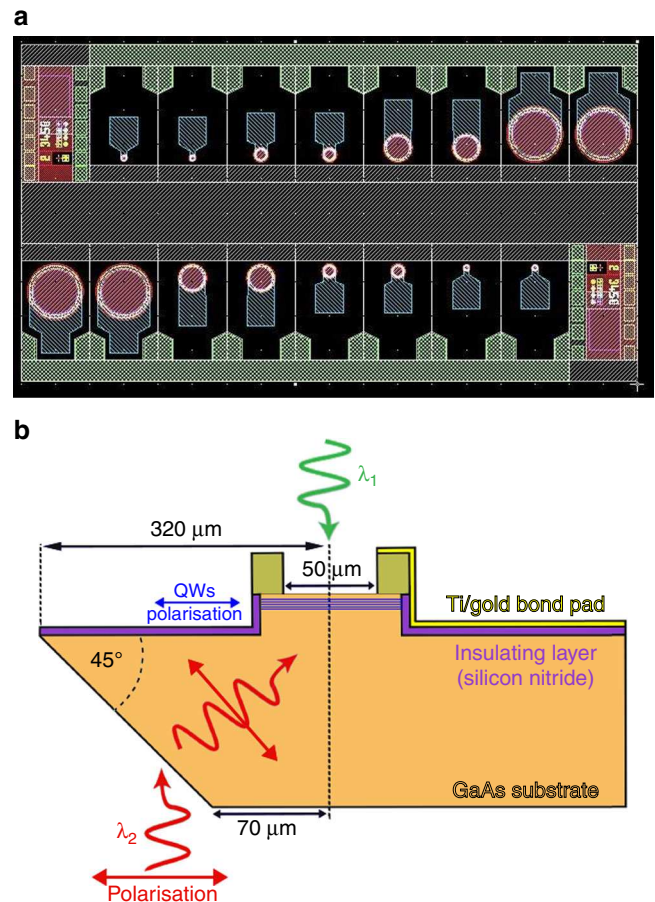


Fig. 6 Device structure. **a** Photolithography schematic used for device fabrication. Green, lower n-type contact pad; blue, upper p-type contacting pad, pink, GaAs window etch. **b** Illumination scheme used to couple the mid-IR radiation into the intraband optical transition

current. The threshold energy for this transition was designed at 0.195 eV so as to be attainable with the available quantum cascade laser sources. This corresponds closely to the $\lambda \sim 6.7 \mu\text{m}/0.185 \text{ eV}$ peak of the measured spectral response of the STPA signal seen in the inset of Fig. 2.

The cascade was optimised for efficient electron transport using an annealing genetic optimisation algorithm, as described in ref. ⁹. A control sample was also grown, with the GaAs in one of the wells (layer 9 in Table 1) replaced with $\text{Al}_{0.3}\text{Ga}_{0.7}\text{As}$ so as to create a 7 nm thick layer to block the QR operation. No STPA photo-current could be detected with this sample.

The grown wafer was processed into devices for opto-electronic characterisation and for the spectroscopy experiments. In order to be transparent to the mid-IR radiation, both the buffer layer and substrate were nominally undoped GaAs. Both the p- and n-contacts had to be formed on the top of the devices, by exposing the n-type layers for metallisation (In-Ge, 20 nm/Au 200 nm) with a partial etch of the wafer. For the p-type metallisations (Au 5 nm/Zn 10 nm/Au 200 nm) we chose to use a series of ring-shaped Ohmic contacts ranging in diameter from 50–400 μm (Fig. 6a). The centres of each of the circular mesas were positioned to align with the centre of the mid-IR beam after it had been refracted by the bevelled substrate. A mesa etch was performed to isolate individual devices and bond pads for both the p- and n-contacts were then formed using Ti, 20 nm/Au, 200 nm. In the case of the bond pad for the p-contacts, an insulating layer of 200 nm silicon nitride was deposited first to prevent shorting of the device (Fig. 6b).

Finally, the GaAs contacting layer (layer number 1 in Table 1) was removed from the optical window of each mesa with another etch.

Quantum mechanical selection rules for excitation of the 2-dimensional intraband transition require a component of the beam with its electric field polarisation normal to the QW planes, so they cannot be driven in a simple normal incidence illumination geometry. For this reason, the wafer was cleaved along a line $\sim 300 \mu\text{m}$ away from the ring mesas (i.e., a distance roughly equal to the substrate thickness) and a 45° chamfered edge was polished into the rear side of the substrate (Fig. 6b). The high ($n = 3.3$) refractive index¹⁶ of the substrate means that on entering the sample from the reverse, the refracted beam travels at an angle close to 45° through the substrate and impinges on the QW's in the device at this

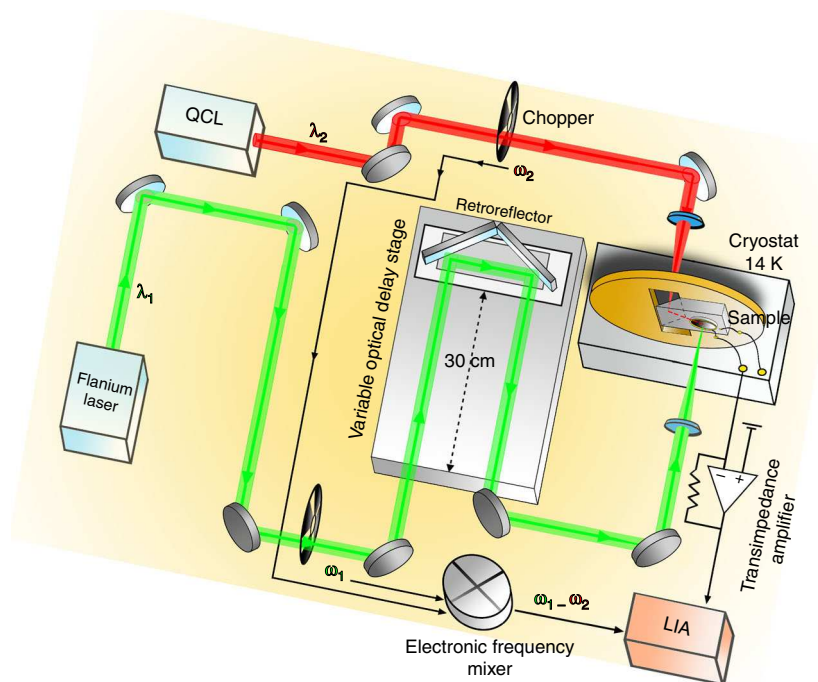


Fig. 7 Schematic of spectroscopy system. The Interband (λ_1) and intraband pulses (λ_2), both tuneable, originating from a fibre supercontinuum source (Fianium) and a quantum cascade laser (QCL) respectively. In the “low frequency” mode (corresponding to all the data presented in the main text) the QCL was triggered, at 100 kHz, using an electronically delayed trigger pulse originating in the fianium laser and both beams were mechanically chopped at ~ 500 Hz. A bespoke frequency mixer circuit was used to generate the difference frequency, $(\omega_1 - \omega_2) \sim 70$ Hz between the two chopping rates to drive a lock-in amplifier that would isolate the STPA photocurrent component

angle. Provided the incident mid-IR is p-polarised, then it can couple to the intraband excitations in this geometry.

A standard TO8 header was modified by drilling a hole through its centre. The devices were mounted and wire bonded with the wedge overhanging the hole in a way that allowed optical access to its rear.

STPA spectroscopy experimental details. Two independently tunable pulsed laser sources were used for the experiment (Fig. 7). Interband excitation was provided by a supercontinuum fibre laser, (Fianium SC450-8-PP). It had a variable repetition rate of 100 kHz–1 MHz. It had a typical maximum pulse energy of 0.4 nJ, a temporal width of 150 ps and bandwidth of 2.5 nm FWHM.

A mid-IR quantum cascade laser (QCL) (Block Engineering “LaserTune”) was used to excite the ISBT transitions. It could be tuned over the wavelength range 6–10 μm , and its repetition rate could be varied in the range 0–100 kHz. The QCL pulse was ~ 100 ns in duration and had a maximum energy of 8 nJ.

Both beams were focused down using 25 mm, f/6 lenses, which generated a spot size which just over-fills the 100 μm device.

The transimpedance amplifier used was a Femto DHPCA-100. It gave a current gain of 10^7 V/A, and had a bandwidth of 1.8 MHz (-3 dB) and rise time of 0.2 μs (10–90%).

The digital mixing circuit was built around a logical AND gate that multiplies the digital values in the square-wave digital frequency reference waveforms generated by each of the optical choppers. It was followed by a third order Butterworth low pass filter chosen for its ability to deliver strong suppression of the fundamental frequencies. It had a -3 dB frequency cutoff at 50 Hz and a -18 dB/octave slope.

Data availability. Data for this report is available from dataenquiryEXSS@imperial.ac.uk.

Received: 26 September 2017 Accepted: 16 January 2018

Published online: 08 March 2018

References

- Okada, Y. et al. Intermediate band solar cells: recent progress and future directions. *Appl. Phys. Rev.* **2**(021302), 1–47 (2015).

- Luque, A. & Martí, A. Increasing the efficiency of ideal solar cells by photon induced transitions at intermediate levels. *Phys. Rev. Letts.* **78**, 5014–5017 (1997).
- Shockley, W. & Queisser, H. J. Detailed balance limit of efficiency of PN junction solar cells. *J. Appl. Phys.* **32**(3), 510–519 (1961).
- Elborg, M. et al. Voltage dependence of two-step photocurrent generation in quantum dot intermediate band solar cells. *Sol. Energy Mater. Sol. Cells* **134**, 108–113 (2015).
- Sugiyama, M. et al. Photocurrent generation by two-step photon absorption with quantum-well superlattice cell. *IEEE J. Photovolt.* **2**, 298–302 (2012).
- Pusch, A. et al. Limiting efficiencies for intermediate band solar cells with partial absorptivity: the case for a quantum ratchet. *Prog. Photo.: Res. Appl.* **24**, 656–662 (2016).
- Luque, A., Martí, A. & Stanley, C. Understanding intermediate-band solar cells. *Nat. Photonics* **6**, 146–152 (2012).
- Yoshida, M., Ekins-Daukes, N. J., Farrell, D. J. & Phillips, C. C. Photon ratchet intermediate band solar cells. *Appl. Phys. Lett.* **10**(263902), 1–4 (2012).
- Curtin, O. J. et al. Quantum cascade photon ratchets for intermediate band solar cells. *J. Photovolt.* **6**(3), 673–678 (2016).
- Levine, B. F. Quantum well infrared photodetectors. *J. Appl. Phys.* **74**(8), R1–R81 (1993).
- Asahi, S., Teranishi, H., Kusaki, K., Kaizu, T. & Kita, T. Two-step photon up-conversion solar cells. *Nat. Comm.* **8**, 14962 (2017).
- Sellers, D. G., Polly, S., Hubbard, S. M. & Doty, M. F. Analyzing carrier escape mechanisms in InAs/GaAs quantum dot p-i-n junction photovoltaic cells. *Appl. Phys. Lett.* **104**(223903), 1–4 (2014).
- Vodopyanov, K. L., Chazapis, V., Phillips, C. C., Sung, B. & Harris, J. S. Jr Intersubband absorption saturation study of narrow III-V Multiple quantum wells in the $\lambda=2.8\text{--}9$ μm spectral range. *Semicond. Sci. Technol.* **12**(6), 708–714 (1997).
- Andersson, J. Y., Lundqvist, L. & Paska, Z. F. Quantum efficiency enhancement of AlGaAs/GaAs quantum well infrared detectors using a waveguide with a grating coupler. *Appl. Phys. Lett.* **58**(20), 2264–2266 (1991).
- Levine, B. F. et al. Photoexcited escape probability, optical gain, and noise in quantum well infrared photodetectors. *J. Appl. Phys.* **72**, 4429–4443 (1992).
- Blakemore, J. F. Semiconducting and other major properties of gallium arsenide. *J. Appl. Phys.* **53**, R123–R181 (1982).

Acknowledgements

This work was funded by the Engineering and Physical Sciences Research Council, under grant reference EP/K029398/1.

Author contributions

N.E.D., N.H., M.F., A.P., C.C.P., A.V.S. and M.Y. contributed to the design of the experiments; N.H., M.F., C.C.P., A.V.S., T.W. and M.Y. contributed to the spectroscopy; O.C., N.H., A.P. and M.Y. to sample modelling; O.C., N.E.D., N.H., A.P., C.C.P. and M.Y. to sample design; E.C. to sample growth; K.K. to device fabrication; N.E.D., O.H. and C. C.P. to project conception and management. All authors participated in the preparation of the manuscript.

Additional information

Supplementary information accompanies this paper at <https://doi.org/10.1038/s42005-018-0007-6>.

Competing interests: The authors declare no competing interests.

Reprints and permission information is available online at <http://npg.nature.com/reprintsandpermissions/>

Publisher's note: Springer Nature remains neutral with regard to jurisdictional claims in published maps and institutional affiliations.



Open Access This article is licensed under a Creative Commons Attribution 4.0 International License, which permits use, sharing, adaptation, distribution and reproduction in any medium or format, as long as you give appropriate credit to the original author(s) and the source, provide a link to the Creative Commons license, and indicate if changes were made. The images or other third party material in this article are included in the article's Creative Commons license, unless indicated otherwise in a credit line to the material. If material is not included in the article's Creative Commons license and your intended use is not permitted by statutory regulation or exceeds the permitted use, you will need to obtain permission directly from the copyright holder. To view a copy of this license, visit <http://creativecommons.org/licenses/by/4.0/>.

© The Author(s) 2018